International Journal of Mechanical Sciences 273 (2024) 109234

Contents lists available at ScienceDirect

International Journal of Mechanical Sciences

journal homepage: www.elsevier.com/locate/ijmecsci

A neural network peridynamic method for modeling rubber-like materials

Yujie Chen [a], Yang Yang [b,*], Yijun Liu [a]

[a] Department of Mechanics and Aerospace Engineering, Southern University of Science and Technology, Shenzhen, Guangdong, China
[b] Faculty of Material Science, Shenzhen MSU-BIT University, Shenzhen, Guangdong 518172, China

ARTICLE INFO

Keywords:
Rubber-like materials
Neural network
Zero-energy modes
Deformation and fracture
Non-ordinary state-based peridynamics

ABSTRACT

Peridynamic (PD) is a powerful tool for simulating the large deformation and failure process of many types of materials. However, its use in modeling rubber-like materials is limited due to the complex constitutive nature of the material, and low efficiency and numerical oscillation caused by PD. To address this issue, a neural network (NN) non-ordinary state-based peridynamics (NOSB PD) method is developed to model the large deformation and failure behavior of rubber-like materials. This method is free of the zero-energy modes, and can significantly improve the computational efficiency. Unlike the traditional NOSB PD method that formulates the force density vector based on the deformation gradient, this method uses a deep NN to map the bond related quantities to the force density vector. The accuracy and efficiency of the proposed method are demonstrated through a series of numerical examples. Additionally, this method can be applied to various hyperelastic materials for which analytical constitutive models exist.

1. Introduction

Peridynamics (PD) is a non-local theory, that has been extensively studied since its inception by Silling [1]. In the PD theory, material points can interact with each other within a certain interaction domain, known as the horizon, which serves as an internal length parameter. The PD equation of motion is an integro-differential equation. The description of damage is straightforward, as it involves removing the interaction of points in the integral [2]. Therefore, the formulation is still valid even when there is an invalid spatial derivative or a discontinuity occurs.

Because of the above-mentioned advantages, PD has proven to be an effective and efficient method for modeling discontinuous problems. Many studies utilized PD techniques to model crack and failure in metal materials [3–5], glass plates [6–8], rock-like materials [9–11] and other brittle materials [12–15]. However, there are limited studies on modeling rubber-like materials using PD methods. One of the reasons for this is that current PD methods face difficulties in accurately and efficiently modeling rubber-like materials.

Bond-based (BB) PD [1–16] theory states that the interaction forces between the paired material points act on the same line with the same magnitude and opposite directions, similar to a spring. BB PD is the most efficient model among the PD frameworks, considering that the bond stretch is the only variable of the bond force density. However, there is a drawback in the BB PD formulation: the Poisson's ratio is fixed at 1/3 for plane stress analysis and 1/4 for plane strain as well as 3D analysis for isotropic linear elastic materials [17]. To simulate the rubber-like materials by BB PD, Silling and Bobaru [18] developed a nonlinear BB model to model hyperelastic membranes. Bang and Madenci [19] derived a nonlinear form of BB PD based on three primary loading conditions of hyperelastic materials: equibiaxial loading, planar loading and uniaxial loading, to predict the nominal stress. Yin et al. developed a nonlinear expression of bond force based on the second Piola-Kirchhoff stress [20]. However, these formulations of the bond force density are associated with a specific loading condition. As a result, it becomes challenging to model complex or mixed loading conditions. Moreover, Bellido et al. [21] have reported that BB PD does not converge to most hyperelastic models when the interaction horizon approaches zero.

The NOSB PD [21–24] theory is also applied to model rubber-like materials. In this theory, the expression of deformation gradient is proposed in an integral form [21]. This makes it easy to connect with the constitutive functions of hyperelastic materials as expressed in the conventional continuum mechanics. It is possible to achieve incompressibility or slight compressibility by restricting the determinant of the deformation gradient tensor. However, the conventional NOSB PD expression of deformation gradient is proved a non-unique mapping between the deformation states of material points and deformation gradient, which can lead to the zero-energy modes causing numerical

* Corresponding author.
E-mail address: yangy2023@smbu.edu.cn (Y. Yang).

https://doi.org/10.1016/j.ijmecsci.2024.109234
Received 4 January 2024; Received in revised form 24 March 2024; Accepted 26 March 2024
Available online 29 March 2024
0020-7403/© 2024 Elsevier Ltd. All rights reserved.

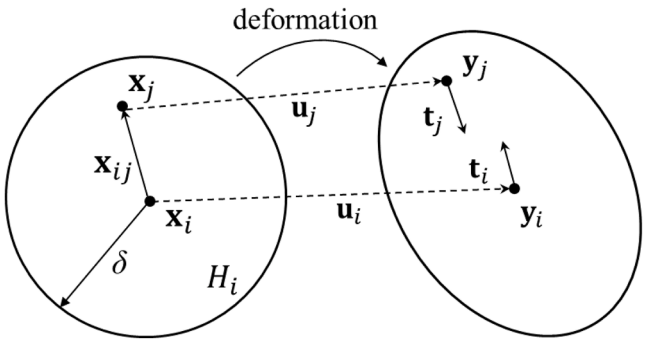

Fig. 1. Peridynamic diagram and notations.

instability and oscillation [25]. To overcome this problem, a few modifications have been proposed, such as supplemental interconnected springs method, average displacement state method and penalty approach [23,26]. These modifications are capable of eliminating the zero-energy modes, but they introduce stabilizing parameters beyond the material parameters in the modification term which may affect the numerical results under large deformation.

In contrast, bond-associated (BA) NOSB model is able to eliminate the zero-energy modes without requiring extra stabilizing parameters [25,27,28]. This is achieved by forming the deformation gradient of a bond at the intersection horizon of two end points. Behera et al. [29] and Roy et al. [30] analyzed the finite elastic deformation and rupture in Neo-Hookean materials as well as polymers predicted by Anand and Talamini-Mao-Anand models, respectively, using the weak form of PD equilibrium equation [31]. This method permits the direct imposing of boundary conditions. Chen et al. studied the fracture of hydrogel with Gent model [32] and fatigue characteristics [33]. However, the calculation of deformation gradient tensor for each bond instead of each material point leads to a relatively high computational cost, especially for 3D case. Therefore, there is a need for a technique that can accurately describe the complex constitutive model of rubber-like materials while effectively eliminating the zero-energy modes to promote the application of NOSB PD.

In recent years, artificial neural networks and machine learning techniques have been applied to facilitate PD methods. For instance, Bekar and Madenci [34] used a sparse linear regression algorithm with peridynamic differential operator (PDDO) proposed by Madenci et al. [35,36] to learn partial differential equations. Haghighat et al. [37] developed a physics-informed deep learning framework with PDDO to capture the elastoplastic response. Yu and Zhou [38] used group method with genetic algorithm to derive the parameters in the BB PD. Ma and Zhou [39] defined the nonlocal influence function (also referred to as the weight function in some literature) by using a data-driven method. You et al. [40] employed a data-driven learning method to combine peridynamics and molecular dynamics to obtain a coarse-grained, homogenized continuum model. Ning et al. [41] achieved the quasi-static BB PD crack simulation using physics-informed neural network frameworks. Babu et al. [42] captured non-local heat conduction using a PD based machine learning model.

In this article, a technique based on neural network is developed within the framework of NOSB PD to simulate the deformation and fracture of rubber-like materials. To generate the training data, various loading conditions were considered. The stretch and rotation of a bond are calculated through the deformation state. Meanwhile, the corresponding force density vector is analytically obtained by using the constitutive relation and the conventional NOSB PD theory. With the help of deep neural network, a nonlinear mapping from the bond stretch and rotation angle to the force density of each bond is achieved. This mapping to calculate the force density vectors not only eliminates the zero-energy modes but also significantly improves the efficiency. The accuracy and high efficiency of the proposed method are demonstrated through a series of numerical examples. The proposed method is general and can be used for various hyperelastic materials with existing analytical constitutive models.

This paper is organized as follows: A brief review of the NOSB PD formulation is presented in Section 2. Section 3 introduces the constitutive model used in this work. Sections 4 and 5 describe the design of the neural network and the process of training data generation, respectively. In Section 6, numerical examples are presented to demonstrate the effectiveness and efficiency of the proposed method.

2. Formulation of non-ordinary state-based peridynamics

Peridynamics is formulated based on non-local theory. By using the meshless implementation, the considered domain is discretized into material points with their own volume and material properties. As shown in Fig. 1, the position vector of a material point in the reference and current configuration are denoted by $\mathbf{x}_i$ and $\mathbf{y}_i$, respectively. Material point $\mathbf{x}_i$ interacts with each neighborhood points $\mathbf{x}_j$ within its horizon H_i. The equation of motion for material point $\mathbf{x}_i$ can be written as:

$$\rho_i \ddot{\mathbf{x}}_i = \int_{H_i} \left(\mathbf{t}_i - \mathbf{t}_j\right) dV_j + \mathbf{b}_i. \tag{1}$$

Here ρ is the mass density. $\ddot{\mathbf{x}}$ is the acceleration vector, and $\mathbf{b}$ is the body force vector. Vector $\mathbf{t}_i$ and $\mathbf{t}_j$ are the pair-wise force density vectors. The force density vector takes the form:

$$\mathbf{t}_i = w(|\mathbf{x}_{ij}|)\mathbf{P}_i \mathbf{K}_i^{-1} \mathbf{x}_{ij}. \tag{2}$$

Here and thereafter, no summation is assumed for repeated index. Vector $\mathbf{x}_{ij} = \mathbf{x}_j - \mathbf{x}_i$ is the bond vector. w is a scalar-valued weight function used for evaluating the contribution of the neighborhood points. In this article, $w = \delta/|\mathbf{x}_{ij}|$ with δ being the radius of H_i. For various options of weight functions, please refer to Ref. [43]. Tensor $\mathbf{P}$ is the first Piola-Kirchhoff stress tensor expressed as:

$$\mathbf{P}_i = \frac{\partial \Psi}{\partial \mathbf{F}_i}, \tag{3}$$

in which Ψ is the strain energy density function. The point-associated deformation gradient tensor $\mathbf{F}$ is obtained by:

$$\mathbf{F}_i = \int_{H_i} w\left(\mathbf{y}_{ij} \otimes \mathbf{x}_{ij}\right) dV_j \cdot \mathbf{K}_i^{-1}, \tag{4}$$

where $\mathbf{K}$ is the shape tensor:

$$\mathbf{K}_i = \int_{H_i} w\left(\mathbf{x}_{ij} \otimes \mathbf{x}_{ij}\right) dV_j. \tag{5}$$

3. Constitutive model for rubber-like materials

Rubber-like materials are often described using hyperelastic models. The strain energy density function Ψ of the hyperelastic model is usually expressed as a function of the invariants (I_1,I_2,I_3) of the right Cauchy-Green strain tensor. For example, Neo-Hookean [44] model is described by the first term of the series linear in I_1. Mooney-Rivlin [45,46] model is constituted by the first and second terms linear in I_1 and I_2. Some other models use the combinations of higher order invariants to capture the large-stretch response [49,52]. In the presented study, the Neo-Hookean model is taken as an example in the analysis.

In Neo-Hooken model, the strain energy density function is expressed as [44]:

$$\Psi = \frac{\mu}{2}(\bar{I}_1 - 3) + \frac{K}{8}\left(J - J^{-1}\right)^2, \tag{6}$$

where μ is the shear modulus, $\bar{I}_1$ the normalized first invariant of right Cauchy-Green strain tensor which is written as $\bar{I}_1 = tr\mathbf{C}J^{-2/3}$, with $\mathbf{C} = \mathbf{F}^T\mathbf{F}$ and $J = \det\mathbf{F}$. Parameter K represents the bulk modulus. The slightly

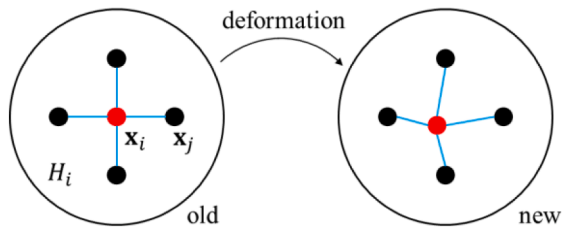

Fig. 2. Illustration of zero-energy modes.

compressible model leads to a relatively large K compared to shear modulus. In this article, K is set as 100 times the shear modulus. The first Piola–Kirchhoff stress tensor can be expressed as:

$$\mathbf{P} = \frac{\partial \Psi}{\partial \mathbf{F}} = \mu\left(\mathbf{F} - \frac{1}{3} tr\mathbf{C}\mathbf{F}^{-T}\right) J^{-2/3} + \frac{K}{4}\left(J^2 - J^{-2}\right)\mathbf{F}^{-T}. \tag{7}$$

In the presented work, the plane stress assumption is considered. Then, the expression of the first Piola–Kirchhoff stress tensor is given in Ref. [29]:

$$\mathbf{P} = \mu\left(\widetilde{\mathbf{F}} - C_{33}\widetilde{\mathbf{F}}^{-T}\right) C_{33}^{-1/3}\widetilde{J}^{-2/3}, \tag{8}$$

where $\widetilde{J} = \det\widetilde{\mathbf{F}}$ with $\widetilde{\mathbf{F}}$ being the in-plane deformation gradient tensor. C_{33} is a component of the right Cauchy-Green strain tensor $\mathbf{C}$, which can be obtained numerically through the equation [29]:

$$\mu\left(\frac{2}{3}C_{33}^{-2/3} - \frac{1}{3}C_{33}^{-1/3} tr\widetilde{\mathbf{C}}\right)\widetilde{J}^{-2/3} + \frac{K}{4}\left(C_{33}\widetilde{J}^2 - C_{33}^{-1}\widetilde{J}^{-2}\right) = 0. \tag{9}$$

4. Stretch-related force density and the desired mapping

For a given loading condition, the force density vector in the conventional NOSB PD is totally determined by the deformation gradient tensor (see Eqs. (2) and (3)). However, this framework suffers from zero-energy modes. This means that different displacement states of material points can be mapped into the same deformation gradient tensor. For instance, consider a 2D regular uniform discretization with a circle horizon, as shown in Fig. 2. A single point movement is applied at point $\mathbf{x}_i$. The deformation gradient of the source point $\mathbf{x}_i$ at the new state is calculated as:

$$\begin{aligned}\mathbf{F}_{i,new} &= \int_{H_i} w\cdot\left[\left(\mathbf{y}_{ij,new}\right)\otimes\left(\mathbf{x}_{ij}\right)\right] dV_j\cdot\mathbf{K}_i^{-1} \\ &= \int_{H_i} w\cdot\left[\left(\mathbf{y}_{ij,old} - \mathbf{u}_i\right)\otimes\mathbf{x}_{ij}\right] dV_j\cdot\mathbf{K}_i^{-1} \\ &= \mathbf{F}_{i,old} - \mathbf{u}_i \otimes \int_{H_i} w\cdot\left(\mathbf{x}_{ij}\right) dV_j\cdot\mathbf{K}_i^{-1}\end{aligned} \tag{10}$$

The integral term on the right-hand side of Eq. (10) becomes zero due to the symmetry of the horizon. As a result, this form of deformation cannot cause a change in deformation gradient. The strain energy density also remains unaltered since the deformation gradient is the only variable in its expression. Consequently, zero-energy modes occur. Ref. [25] provides a similar example that illustrates the zero-energy modes. One of the solutions is to introduce a complementary force density, and regard the bonds as fictitious springs. The stretch of these fictitious springs can change the strain energy density. Thus, the zero-energy modes are avoided. However, the complementary part needs a stabilizing parameter or a penalty factor, which can significantly affect the numerical results under large deformation.

Bond-associated (BA) NOSB model is another solution that can eliminate the zero-energy modes without requiring extra stabilizing parameters [25,27,28]. This is achieved by forming the deformation gradient of a bond at the intersection horizon of two endpoints. Therefore, the formulation of the BA NOSB PD is briefly recalled here. The subscript "ξ" means the quantity is bond-associated. For a bond pointing from material point i to material point j, the deformation gradient associated with the bond is formed considering the information of H_i and H_j expressed as [28,53]:

$$\mathbf{F}_\xi = \left[\int_{H_i\cap H_j} w(\mathbf{y}_k - \mathbf{y}_i)\otimes(\mathbf{x}_k - \mathbf{x}_i) dV_k\right]\mathbf{K}_\xi^{-1}, \tag{11}$$

where the shape tensor associated with the bond is expressed as:

$$\mathbf{K}_\xi = \int_{H_i\cap H_j} w(\mathbf{x}_k - \mathbf{x}_i)\otimes(\mathbf{x}_k - \mathbf{x}_i) dV_k. \tag{12}$$

The force density vector of the bond takes the form [54]:

$$\mathbf{t}_\xi = \frac{1}{2}\frac{\phi_\xi\left(\mathbf{x}_i, \mathbf{x}_j\right)}{\phi\left(\mathbf{x}_i, \mathbf{x}_j\right)} w\mathbf{P}_\xi\mathbf{K}_\xi^{-1}\mathbf{x}_{ij}, \tag{13}$$

with

$$\phi\left(\mathbf{x}_i, \mathbf{x}_j\right) = \frac{\int_{H_i} dV_k}{\int_{H_i} dV_k + \int_{H_j} dV_k} \tag{14}$$

and

$$\phi_\xi\left(\mathbf{x}_i, \mathbf{x}_j\right) = \frac{\int_{H_i\cap H_j} dV_k}{\int_{H_i} dV_k}. \tag{15}$$

In this article, a new method to avoid the zero-energy modes is proposed. As is performed by the fictitious spring modification, if the force density vector is partially determined by the bond stretch instead of solely relying on the deformation gradient, the zero-energy modes can be overcome. Inspired by this, a direct mapping from the bond stretch and bond rotation (along with a few other variables) to the force density vector is constructed.

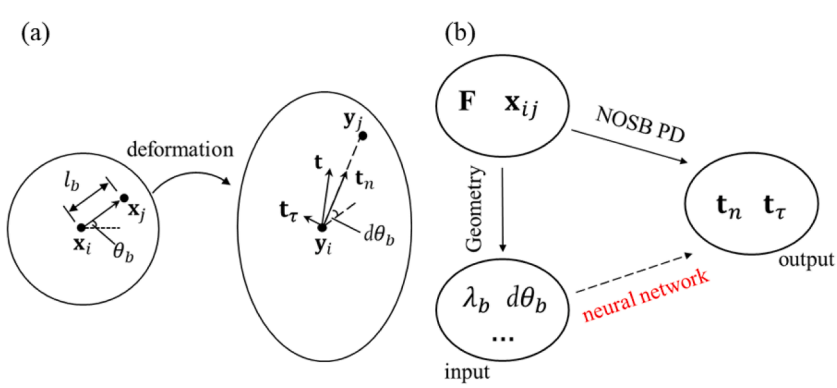

Fig. 3. (a) Notations of bond related quantities during deformation. (b) Illustration of the desired mapping.

Algorithm 1
Pserudocode for generating training data.

```
for various λ1 and λ2
  build the in-plane deformation gradient tensor F
  for various bond length l_b ∈ (0, δ]
    for various bond orientation θ_b ∈ (0, 2π]
      bond vector is (l_b cosθ_b, l_b sinθ_b)^T
      calculate C33 by Eq. (9)
      calculate stress tensor P by Eq. (8)
      calculate force density vector t by Eq. (2)
      decompose t into t_n and t_τ
      calculate bond stretch λ_b and rotation angle dθ_b
      write input data: X_b, dθ_b, l_b, C33, detF
      write output data: |t_n |, |t_τ |
    end
  end
end
```

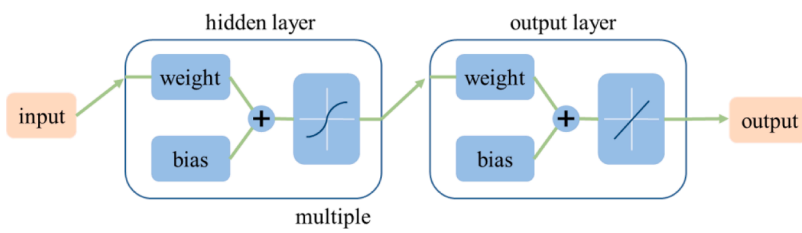

Fig. 4. Illustration of the neural networks.

The in-plane deformation gradient tensor takes the form:

$$\mathbf{F}_{plane} = \begin{bmatrix} \lambda_1 & 0 \\ 0 & \lambda_2 \end{bmatrix}, \tag{16}$$

where λ_1 and λ_2 represent the in-plane principal stretches. For a given deformation gradient $\mathbf{F}$, various bond lengths and orientations are considered. With the information of deformation gradient $\mathbf{F}$ and a particular bond vector, the corresponding bond length $|\mathbf{x}_{ij}|$, the bond stretch λ_b and the bond rotation $d\theta_b$ can be obtained through the geometric relation. The bond stretch is expressed as:

$$\lambda_b = \frac{|\mathbf{y}_{ij}|}{|\mathbf{x}_{ij}|}, \tag{17}$$

where $\mathbf{y}_{ij} = \mathbf{F}_i\mathbf{x}_{ij}$. The rotation angle is calculated as:

$$d\theta_b = \arcsin\left(\frac{\mathbf{x}_{ij} \times \mathbf{y}_{ij}}{|\mathbf{x}_{ij}|\cdot|\mathbf{y}_{ij}|}\right). \tag{18}$$

Meanwhile, the corresponding force density $\mathbf{t}$ of this bond can be calculated by the NOSB PD formulation (Eq. (2)). Then, the force density vector is decomposed into $\mathbf{t}_n$ and $\mathbf{t}_\tau$, which are along the direction of the deformed bond and tangent to the deformed bond respectively, as shown in Fig. 3(a). Note that the positive direction of $\mathbf{t}_n$ is pointing form $\mathbf{y}_i$ to $\mathbf{y}_j$, and counter-clockwise direction is defined as the positive direction of θ and $\mathbf{t}_\tau$.

To find the mapping from the bond related variables to the force density vector, a deep neural network with λ_b, $d\theta_b$, bond length l_b ($l_b = |\mathbf{x}_{ij}|$), C_{33} and det$\mathbf{F}$ as the input, $\mathbf{t}_n$ and $\mathbf{t}_\tau$ as the output is constructed. The process is illustrated in Fig. 3(b). For simplicity, the spatial discretization size dx and its horizon radius δ are fixed at 0.02 cm and $\delta = 3.15\ dx$ for this study.

5. Generation of training data

The pseudocode for generating training data is shown in Algorithm 1. Various loading conditions including but not limited to uniaxial tension, pure shear test or biaxial tension are considered. Parameters λ_1 and λ_2 are set from 0.8 to 4.0 respectively, which covers standard deformation states of rubber-like materials in plane stress case. The shear modulus and bulk modulus are set 1 and 100 respectively. The neural network structure is illustrated in Fig. 4, with five neurons as the input and two neurons as the output. Note that the tensors in the algorithm are all for 2D case.

Considering a wide range of deformation stated and bond vector, around 10,000 samples are generated in the training data. The training process is carried out using the Neural Net Fitting tool on Matlab (R2023b, MathWorks, USA). The number of hidden layers and output layers are set to 20 and 2, respectively. The Sigmoid function is applied to each hidden layer as the activation function. The Levenberg-Marquardt algorithm [50,51] is the training function. 70% of the dataset is used to train the model, while15% is reserved for both validation and prediction. There is no noise in the process of generating training data, since all the quantities are obtained from pure mathematical formulas. Therefore, the trained NN achieves a high accuracy of around 99%.

The method used to construct the training data and select input neurons is not restricted. For instance, the horizon radius δ can be set to 1 in the training data. The bond length l_b of the input neurons can be non dimensionalized as l_b/δ. Then in the actual numerical implementation, the force density predicted by the NN needs to be multiplied by a factor to satisfy different horizon sizes. And one can deduce that the factor is related to the value of the shape tensor and the actual bond length (Eq. (2)). Additionally, if the weight function is adjusted to eliminate the bond force density's dependence on the bond length, the neuron l_b can be removed, resulting in improved efficacy of the trained NN. There are many other forms of construction of the NN that need to be explored further.

6. Numerical examples

6.1. Procedure and implementation

In the PD implementation, the considered domain is discretized uniformly into material points. The equation of motion is rewritten as:

Algorithm 2
Pseudocode for PD implementation.

```
Preparation: Discrete the model and create arrays to store the initial position vector x, deformed position vector y, displacement vector u.
Search and store the neighborhood points for each material point.
Build an input matrix in dimension n_total_bond × 5 (λb,dθ, lb C33, detF), and an output matrix in dimension n_total_bond × 2 (|tn |, |tr |).
for tt = 1: max_time_step
  apply the boundary conditions
  calculate the deformation gradient for each node (Eq. (15))
  calculate C33(i), detFi and dθHi for each node
  for i = 1: total_node
    for j = l: n_neighbor
      calculate λb, dθb and lb for the bond
      write the λb, dθ, lb,C33 and detF to the certain row of input matrix
    end
  end
  use the neural network to map the input matrix to the output matrix
  assemble the tn and tr to each material point
  update the position of material points by kinetic equation
end
```

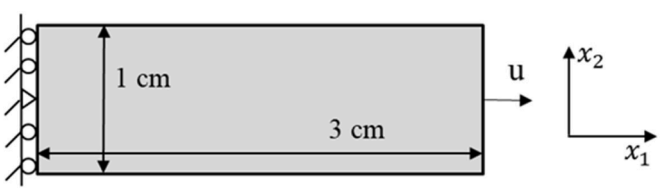

Fig. 5. Geometry and boundary conditions of the uniaxial test.

$$\rho_i \ddot{\mathbf{u}}_i = \sum_{j \in H_i} (\mathbf{t}_i - \mathbf{t}_j) V_j + \mathbf{b}_i. \tag{19}$$

Eq. (4) is rewritten as

$$\mathbf{F}_i = \sum_{j \in H_i} w(\mathbf{y}_{ij} \otimes \mathbf{x}_{ij}) V_j \cdot \mathbf{K}_i^{-1}, \tag{20}$$

with shape tensor $\mathbf{K}_i$ being

$$\mathbf{K}_i = \sum_{j \in H_i} w(\mathbf{x}_{ij} \otimes \mathbf{x}_{ij}) V_j. \tag{21}$$

The detailed implementation procedures are shown in Algorithm 2. To optimize performance, the input data for each bond is consolidated into an input matrix. The input matrix is then fed into the trained NN model at each time step. It is not recommended to call the trained NN model for each bond individually as this could significantly increase processing time.

It should be noticed that, the C_{33} and det**F** in the input matrix are set as $C_{33} = (C_{33(i)} + C_{33(j)})/2$ and $\det\mathbf{F} = (\det\mathbf{F}_i + \det\mathbf{F}_j)/2$. The term $d\theta$ is modified as $d\theta = d\theta_b - (d\theta_{H_i} + d\theta_{H_j})/2$. Here, $d\theta_H$ is the rotation angle of the horizon which can be obtained from the deformation gradient tensor as:

$$d\theta_{H_i} = 0.5\left[\arcsin\left(G_{(1)1}g_{(1)2} - G_{(1)2}g_{(1)1}\right) + \arcsin\left(G_{(2)1}g_{(2)2} - G_{(2)2}g_{(2)1}\right)\right], \tag{22}$$

with

$$\begin{aligned}
\mathbf{G}_{(1)} &= \left[G_{(1)1}G_{(1)2}\right]^T = [1 \quad 0]^T \\
\mathbf{G}_{(2)} &= \left[G_{(2)1}G_{(2)2}\right]^T = [0 \quad 1]^T \\
\mathbf{g}_{(1)} &= \begin{bmatrix} g_{(1)1} \\ g_{(1)2} \end{bmatrix} = \begin{bmatrix} F_{11} \Big/ \sqrt{F_{11}^2 + F_{21}^2} \\ F_{21} \Big/ \sqrt{F_{11}^2 + F_{21}^2} \end{bmatrix} \\
\mathbf{g}_{(2)} &= \begin{bmatrix} g_{(2)1} \\ g_{(2)2} \end{bmatrix} = \begin{bmatrix} F_{12} \Big/ \sqrt{F_{12}^2 + F_{22}^2} \\ F_{22} \Big/ \sqrt{F_{12}^2 + F_{22}^2} \end{bmatrix}
\end{aligned} \tag{23}$$

It is important to note that bond rotation is relative to its horizon and is not affected by rigid body rotation. Therefore, $d\theta_H$ should be calculated. The vectors **G** and **g** refer to the convected basis vectors, which are also used in Refs. [47,48]. When generating training data, the shape tensor **K** is theoretically calculated on a circular horizon. However, in PD implementation, the discretization brings some error when calculating the shape tensor. Furthermore, the material points located on the edge or at the corner do not have a complete circular horizon. Therefore, some modifications should be made. The force density vector is modified as:

$$\mathbf{t}_{modified} = \frac{fac_i + fac_j}{2} \mathbf{t}_{nn}, \tag{24}$$

where $\mathbf{t}_{nn}$ is the output of the trained neural network. The factor *fac* is formed based on the value of the shape tensor, expressed as:

$$fac_i = \frac{2\int_{circularhorizon} w(|\mathbf{x}_{ij}|)\mathbf{x}_{ij,1}^2 dV_j}{\sum_{j \in H_i} w(|\mathbf{x}_{ij}|)\mathbf{x}_{ij,1}^2 V_j + \sum_{j \in H_i} w(|\mathbf{x}_{ij}|)\mathbf{x}_{ij,2}^2 V_j}, \tag{25}$$

with $\mathbf{x}_{ij,1}$ and $\mathbf{x}_{ij,2}$ representing the components of the bond vector $\mathbf{x}_{ij}$.

In this section, some numerical examples are analyzed to illustrate the accuracy and efficiency of the present algorithm. For all the numerical examples, uniform discretization is used with a fixed horizon size of $3.15dx$, where the spatial discretization size dx is fixed at 0.02 cm. The equation of motion is solved using the explicit central difference method. The quasi-static solutions are achieved by introducing a numerical damping term into the equation of motion.

6.2. Uniaxial tension

As shown in Fig. 5, there is a Neo-Hookean sheet with dimension of 3 cm × 1 cm. A displacement is applied on the right edge. The left edge is not allowed to move along the x_1 direction and its midpoint is fixed to prevent the rigid motion. The shear modulus is 1.0 kPa with bulk modulus being 100.0 kPa. The sheet is stretched at three different

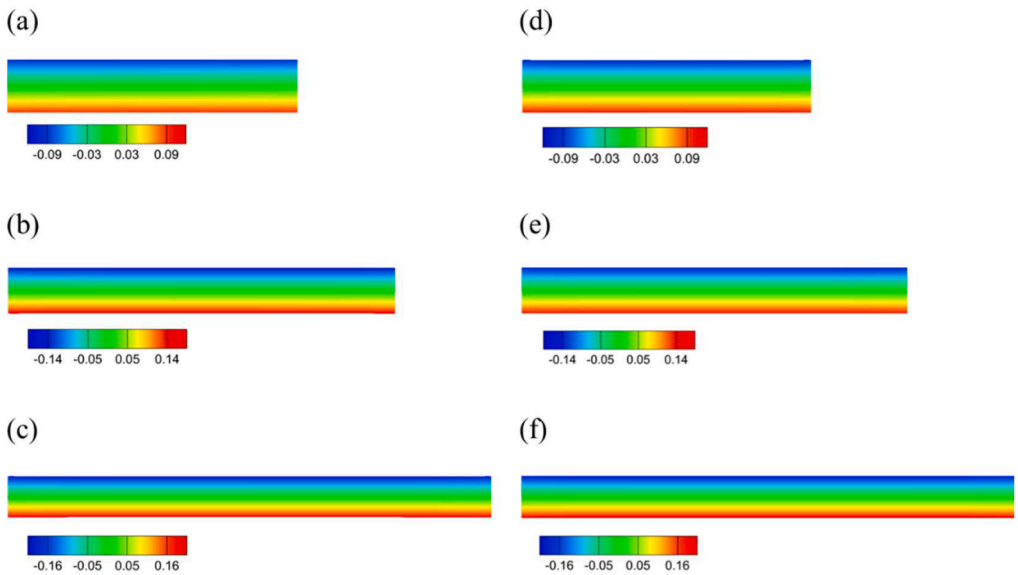

Fig. 6. Vertical displacement contours of the deformed sheet for λ=1.5, 2.0 and 2.5 respectively. (a)-(c): NN NOSB PD results. (d)-(e): BA NOSB PD results. The unit is centimeter.

Table 1
The comparison of the vertical displacement and nominal stress between theoretical prediction and NN NOSB PD prediction.

stretch	u_2_PD (cm)	u_2_theory (cm)	Error (%)	stress_PD (kPa)	stress_theory (kPa)	Error (%)
1.5	0.0915	0.0918	0.33	1.09	1.06	3.26
2.0	0.145	0.146	0.68	1.80	1.75	2.86
2.5	0.182	0.184	1.09	2.40	2.34	2.56

stretch ratio, $\lambda = 1.5$, 2.0 and 2.5, where λ is the ratio of the current length to the initial length along the loading direction. The simulations are carried out using the proposed NN NOSB PD and the BA NOSB PD respectively. The contours of the vertical displacement are plotted in Fig. 6.

For uniaxial tension, the principal stretches are λ, $\lambda^{-1/2}$ and $\lambda^{-1/2}$. Thus, the strain energy density can be expressed as

$$\Psi_{uniaxial} = \frac{\mu}{2}\left(\lambda^2 + 2\lambda^{-1} - 3\right). \tag{26}$$

The nominal stress along the loading direction is expressed as [55]:

$$s = \frac{\partial \Psi_{uniaxial}}{\partial \lambda} = \mu\left(\lambda - \lambda^{-2}\right). \tag{27}$$

The theoretical prediction of u_2 can be obtained setting the vertical stretch as $\lambda^{-1/2}$, where u_2 is the displacement of the bottom edge along x_2 direction. The comparisons of the PD predictions and theoretical predictions are presented in Table 1. The error is defined as:

$$error = \frac{|value_{theory} - value_{PD}|}{value_{theory}} \times 100\%. \tag{28}$$

The results show that all errors are within 3.5%, which demonstrates the capability of the model to accurately capture the stress and slight compressibility under uniaxial loading. The main source of the error is

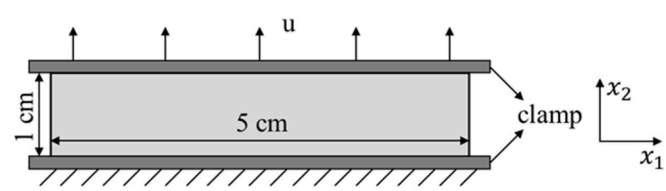

Fig. 7. Geometry and boundary conditions of the pure shear test.

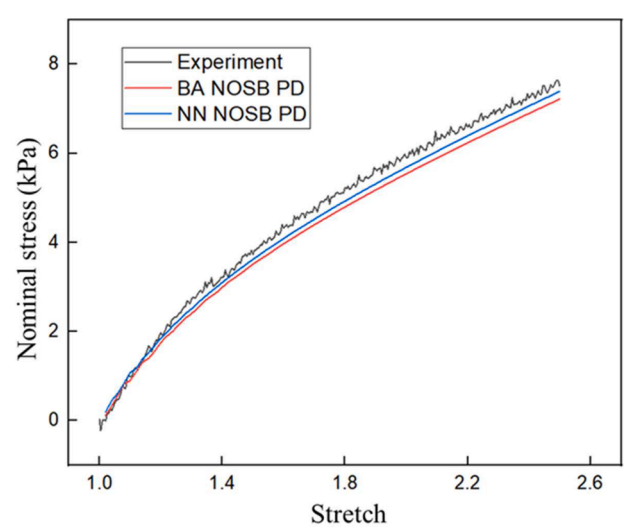

Fig. 8. Comparison of the nominal stress predicted by PD model and measured by experiment.

Table 2
Comparisons of time consumed by NN NOSB PD and BA NOSB PD.

λ=1.5 (1000 steps)			λ=2.0 (1500 steps)			λ=2.5 (2000 steps)		
time_NN	time_BA	ratio	time_NN	time_BA	ratio	Time_NN	time_BA	ratio
359s	4456s	12.4	535s	6825s	12.8	708s	9173s	13.0

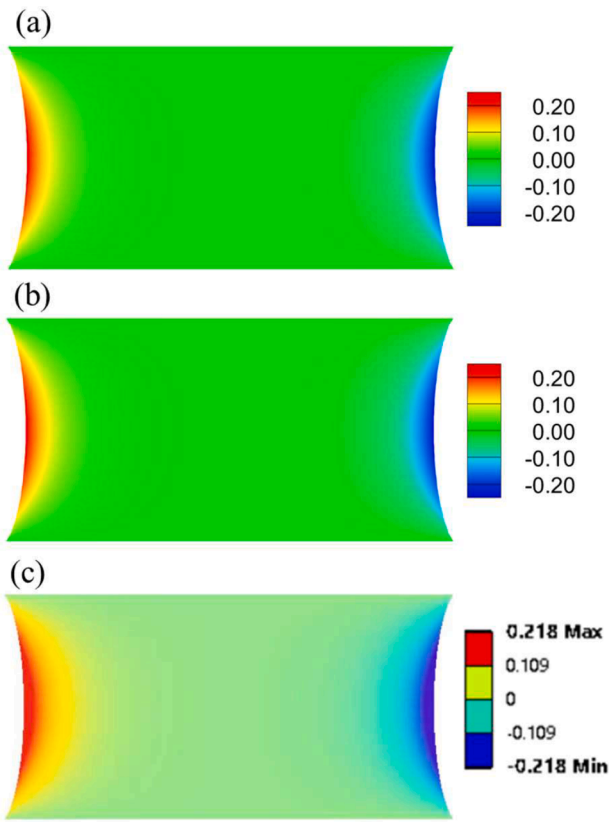

Fig. 9. Horizontal displacement contours of the deformed sheet predicted by (a) NN NOSB PD, (b) BA NOSB PD, (c) FEM. The stretch is 2.5. The unit is centimeter.

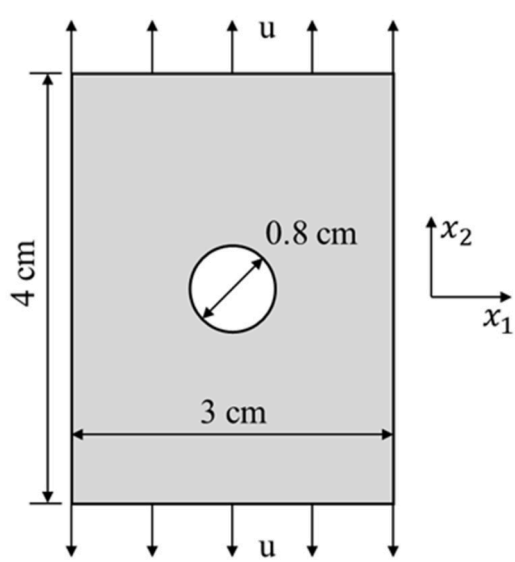

Fig. 10. Geometry and boundary conditions of a sheet with a hole.

due to the boundary effect of PD. The vertical displacements predicted by BA NOSB PD is 0.091 cm, 0.145 cm, 0.181 cm under $\lambda = 1.5$, 2.0 and 2.5, respectively. The corresponding nominal stress are 1.06 kPa, 1.75 kPa and 2.32 kPa.

Matlab (R2023b, MathWorks, USA) programs are developed to run the simulations. The quasi-static solutions are obtained under $\lambda = 1.5$, 2.0, and 2.5 by performing 1000, 1500, and 2000 time steps, respectively. Table 2 lists the time taken by both schemes. In all examples, NN NOSB PD consumed less than one-tenth of the time taken by BA NOSB PD. This suggests that the efficiency disparity can be more significant in 3D cases.

6.3. Pure shear test

A commonly used test for rubber-like materials is the pure shear test. In this section, a Neo-Hookean sheet measuring 5 cm × 1 cm is tested, as described in Ref. [55]. As shown in Fig. 7, the top edge of the sheet is gradually loaded upward while the bottom edge is fixed. The shear modulus is 3.06 kPa and the bulk modulus is 306.0 kPa. The sheet is loaded to stretch gradually, and the horizontal shrink of the sheet can be neglected. Due to the slight compressibility, the stretch along the thickness direction is around $1/\lambda$. This deformation state can be achieved by shear stress solely, as shown in a Mohr's circle. This type of experiment is called a pure shear test and is widely performed on rubber-like materials [56–58].

Fig. 8 shows the of the nominal stress measured in experiment (Ref. [55]) is compared the stress predicted by the proposed PD model. Using a time step number of 1500, the time consumed by BA NOSB PD is 11,215 s, while NN NOSB PD took 850 s. The ratio is around 13.2. In Fig. 9, the horizontal displacement contours at $\lambda = 2.5$ are predicted by NN NOSB PD, BA NOSB PD and FEM, respectively. The FEM analysis is performed on ANSYS with 12,500 quadratic quadrilateral elements. The maximum horizontal displacement predicted by NN NOSB PD is around 0.211 cm. This is compared with 0.218 cm calculated by FEM. The deviation is 3.2%.

6.4. Tension of a sheet with a hole

As is shown in Fig. 10, the Neo-Hookean sheet is measured to be 4 cm × 3 cm in size. Tensile displacement is applied to the top and bottom in opposite directions, both with a magnitude of 0.4 cm ($\lambda = 1.2$). There is a hole in the center of the sheet with a diameter of 0.8 cm. The shear modulus and bulk modulus are 1.0 kPa and 100.0 kPa, respectively. The vertical displacement contours predicted by NN OSB PD and FEM are shown in Fig. 11. The FEM simulation is performed on ANSYS, using 4662 quadratic quadrilateral elements. The comparison of the horizontal displacement on the left edge, as predicted by the proposed method and FEM, can be seen in Fig. 12. The maximum horizontal displacement is found to be 0.16 cm, with a deviation of 2.5% compared to the FEM prediction.

6.5. Pure shear with a precut

This numerical example is compared to the pure shear tear test that was conducted in Ref. [59]. The geometry and boundary conditions are shown in Fig. 13. The length and width of the sheet are 11 cm and 3 cm, respectively, and its thickness is 2.5 mm. The top edge is gradually displaced while the bottom edge is fixed. The material parameter is calibrated by comparing the elastic response of the sample without cracks, as was done in Ref. [59]. The material is described as a nearly incompressible Neo-Hookean model with a shear modulus of 0.72 MPa.

A history-dependent function is introduced in the force density vector to record the failure of the bonds as:

$$\mathbf{t}_i = \gamma(\lambda_b, t) w\left(\left|\mathbf{x}_{ij}\right|\right) \mathbf{P}_i \mathbf{K}_i^{-1} \mathbf{x}_{ij}, \tag{29}$$

and the history-dependent function is defined as:

$$\gamma(\lambda_b, t) = \begin{cases} 1, \text{if} \lambda_b < \lambda_c \text{forall} 0 \le t' \le t \\ 0, \text{otherwise} \end{cases}, \tag{30}$$

where t is time. If the bond stretch exceeds the critical value λ_c, it will break irreversibly. The damage of a material point is defined as:

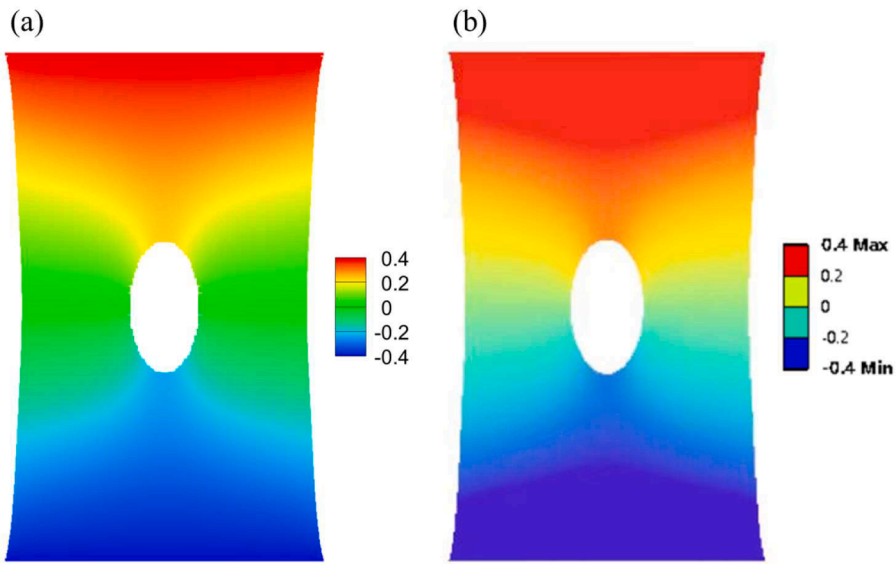

Fig. 11. Vertical displacement of the sheet at $\lambda = 1.2$ predicted by (a) NN NOSBPD, (b) FEM. The unit is centimeter.

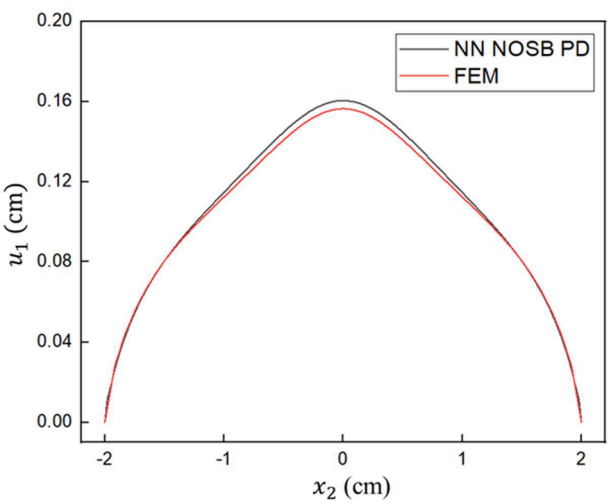

Fig. 12. Comparison of the horizontal displacement on the left edge.

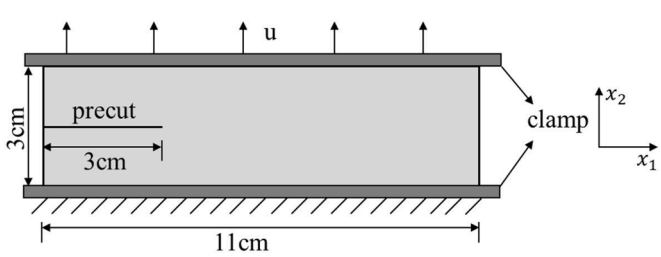

Fig. 13. Geometry and boundary conditions of pure shear test with a precut.

$$dmg_i = 1 - \frac{\int_{H_i} w(|\mathbf{x}_{ij}|)\gamma(\lambda_b, t)dV_j}{\int_{H_i} w(|\mathbf{x}_{ij}|)dV_j}. \tag{31}$$

There are various criteria to determine the bond breakage, including using criteria based on fracture energy [60–62], J-integral based criteria, and stress tensor based criteria [63,64]. For the Mode-I crack of rubber-like materials, the crack tip can be observed as a circular arc and the material near the crack tip is under uniaxial tension [65,66]. Therefore, the failure at the crack tip of hyperplastic material is assumed to occur when bond stretch λ_b exceeds λ_c, which is called the effective stretch criterion for rubber-like material [65]. The value of λ_b can be calibrated by comparing it with the experimental loading curve until rupture [29]. In this particular example, λ_c is set 3.5.

Some crack propagation processes are illustrated in Fig. 14. The crack continues to propagate along a straight line until the sheet is divided into two parts. The predicted loading curve is depicted in Fig. 15, which is very close to the experiment data provided in Ref. [59]. Thus, the proposed NN NOSB PD is validated to model the crack propagation.

6.6. Tension of a sheet with voids and precuts

The Fig. 16 shows the geometry of a Neo-Hookean sheet that has five circular voids with the same diameters, one at the center and the others located symmetrically. The sheet is 4.5 cm × 3.0 cm in size, and there are two precuts on its left and right edges. Displacements are applied to the top and bottom edges to stretch the sheet gradually. For this particular example, λ_c is set 2.0. The crack propagation process is illustrated in Fig. 17. The precuts initially propagate to the voids, and then new cracks develop on the boundary of the central void.

6.7. Modeling Gent material

The proposed method is capable of modeling other hyperelastic models. Except for the Neo-Hooken model, the Gent model is also studied in this work. The strain energy density function of Gent model is written as [52]:

$$\Psi_{\text{Gent}} = -\frac{\mu J_m}{2}\ln\left(1 - \frac{\bar{I}_1 - 3}{J_m}\right) + \frac{1}{D}\left(\frac{J^2 - 1}{2} - \ln J\right). \tag{32}$$

The stretch limit parameter J_m defines the stiffer response under large tensile stretch. For slight compressibility, parameter D should be set relatively small. The same NN strategy can learn different non-linear behavior automatically. In this example, uniaxial tension is performed on a sheet with the same geometry as in Section 6.2. The shear modulus is 1.0 kPa. Parameter D is 0.01 $(\text{kPa})^{-1}$ and J_m is 120.

For uniaxial tension, the principal stretches are λ, $\lambda^{-1/2}$ and $\lambda^{-1/2}$. Thus, the strain energy density can be expressed as:

$$\Psi_{uniaxia} = -\frac{\mu J_m}{2}\ln\left(1 - \frac{\lambda^2 + 2\lambda^{-1} - 3}{J_m}\right). \tag{33}$$

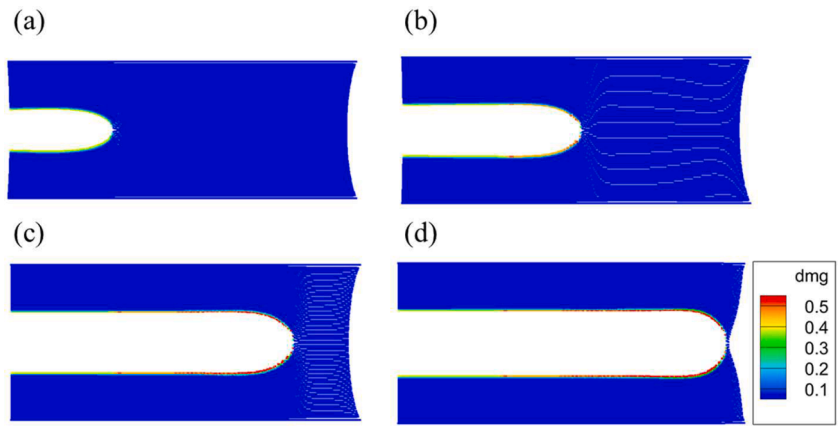

Fig. 14. PD prediction of the crack propagation of the sheet.

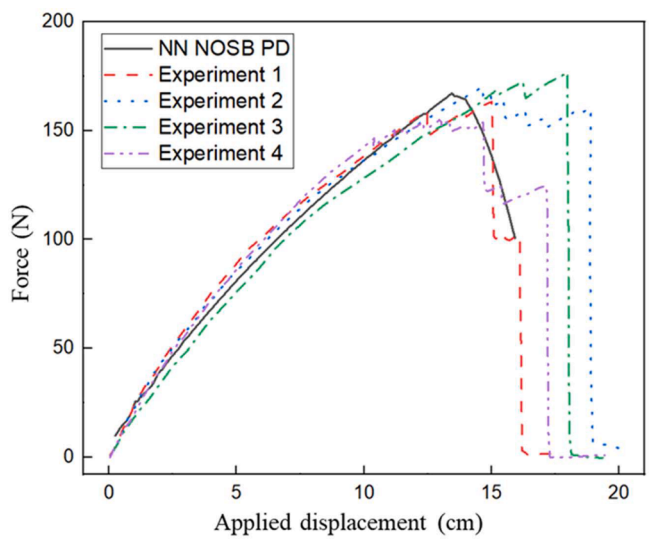

Fig. 15. Comparison of the loading curve predicted by PD and experiment data.

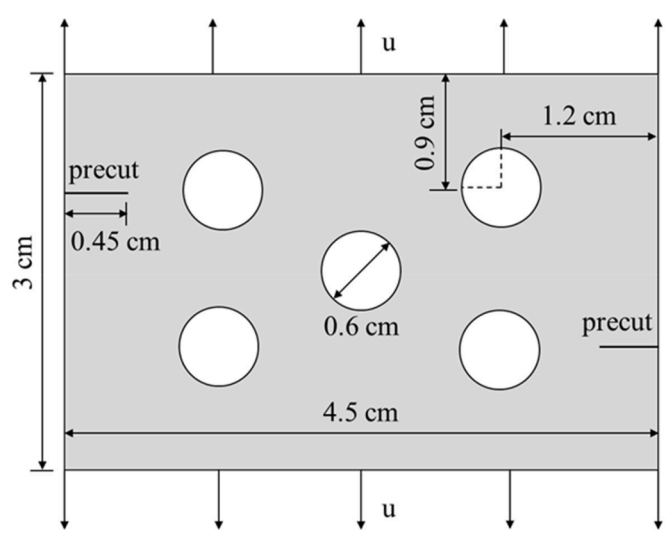

Fig. 16. Geometry and boundary conditions of a sheet with voids and precuts.

The nominal stress along the loading direction is written as [32]:

$$s = \frac{\partial \Psi_{uniaxial}}{\partial \lambda} = \frac{\mu J_m \left(\lambda - \lambda^{-2}\right)}{J_m - \lambda^2 - 2\lambda^{-1} + 3}. \tag{34}$$

As J_m increases to infinity, this expression recovers that of the Neo-Hookean model (Eq. (27)).

The Fig. 18 shows the vertical displacement contour provided by the NN NOSB PD at $\lambda = 2.0$. By setting the vertical stretch, the calculated vertical displacement on the bottom edge is 0.146 cm. The average vertical displacement on the bottom edge, as predicted by PD is 0.145 cm. The deviation from the theoretical value is only 0.7%. According to PD prediction, the nominal stress along the loading direction is 1.83 kPa, whereas the theoretical value is 1.78 kPa. The error from the theoretical value is 2.8%.

7. Conclusions

In this paper, a new algorithm for modeling the large deformation and failure of rubber-like materials is proposed. The algorithm is based on a neural network and NOSB PD. The constitutive function of rubber-like materials can be directly introduced in the governing equation of NOSB PD by the first Piola-Kirchhoff stress. A deep neural network technique is used to achieve a novel mapping between the deformation state and the force density vector in the PD framework. This technique can avoid the zero-energy modes and greatly improve the efficiency. The accuracy of the proposed method is validated through comparisons with FEM results and experiment data. The proposed NN NOSB PD is general enough for various hyperelastic models. Extending it to model 3D problems would be interesting and demonstrate more advantages of the proposed NN NOSB PD.

CRediT authorship contribution statement

Yujie Chen: Writing – original draft, Data curation. **Yang Yang:** Writing – review & editing, Writing – original draft, Supervision, Methodology, Conceptualization. **Yijun Liu:** Writing – review & editing, Supervision.

Declaration of competing interest

The authors declare that they have no known competing financial interests or personal relationships that could have appeared to influence the work reported in this paper.

Data availability

Data will be made available on request.

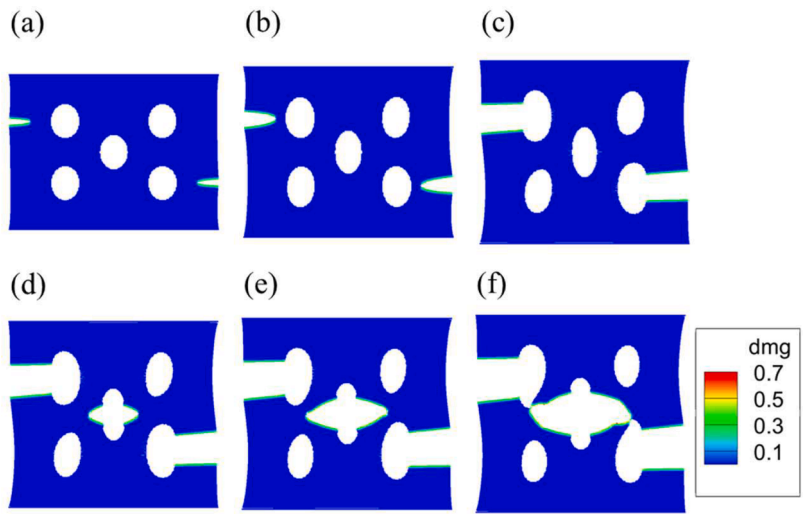

Fig. 17. PD prediction of the crack propagation and initiation of the sheet.

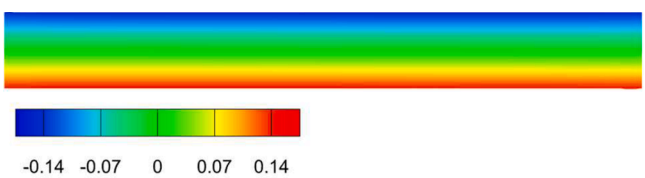

Fig. 18. Vertical displacement contour of the deformed sheet. The stretch is 2.0. The unit is centimeter.

Acknowledgments

The authors would like to thank the financial support from the National Natural Science Foundation of China (Project Nos. 12272160 and 12372198) and the Shenzhen National Science Foundation (Project No. 20231129213819001).

References

[1] Silling SA. Reformulation of elasticity theory for discontinuities and long-range forces. J Mech Phys Solids 2000;48:175–209.
[2] Silling SA, Askari E. A meshfree method based on the peridynamic model of solid mechanics. Comput Struct 2005;83:1526–35.
[3] Ren B, Wu CT, Askari E. A 3D discontinuous Galerkin finite element method with the bond-based peridynamics model for dynamic brittle failure analysis. Int J Impact Eng 2017;99:14–5.
[4] Ghorbel O, Koubaa S, Mars J, Wali M, Dammak F. Non associated-anisotropic plasticity model fully coupled with isotropic ductile damage for sheet metal forming applications. Int J Solid Struct 2019;166:96–111.
[5] Wang H, Wu L, Guo J, et al. Numerical analysis on failure of sheet metals with non-ordinary state-based peridynamics. Eng Fract Mech 2023;292:109652.
[6] Bobaru F, Ha YD, Hu W. Damage progression from impact in layered glass modeled with peridynamics. Open Eng 2012;2(4):551–61.
[7] Hu W, Wang Y, Yu J, Yen CF, Bobaru F. Impact damage on a thin glass plate with a thin polycarbonate backing. Int J Impact Eng 2013;62:152–65.
[8] Jafaraghaei Y, Yu T, Bui TQ. Peridynamics simulation of impact failure in glass plates. Theor Appl Fract Mech 2022;121:103424.
[9] Demmie PN, Silling SA. An approach to modeling extreme loading of structures using peridynamics. J Mech Mater Struct 2007. https://doi.org/10.2140/jomms.2024.19-2.
[10] X.P. Zhou, X.B. Gu, Y.T. Wang, Numerical simulations of propagation, bifurcation and coalescence of cracks in rocks 80(2015)241–54.
[11] Ha YD, Lee J, Hong JW. Fracturing patterns of rock-like materials in compression captured with peridynamics. Eng Fract Mech 2015;144:176–93.
[12] Ha YD, Bobaru F. Characteristics of dynamic brittle fracture captured with peridynamics. Eng Fract Mech 2011;78:1156–68.
[13] Rahimi MN, Kefal A, Yildiz M. An improved ordinary-state based peridynamic formulation for modeling FGMs with sharp interface transitions. Int J Mech Sci 2021;197:16322.
[14] Friedrich LF, Colpo AB, Kosteski LE, et al. A novel peridynamic approach for fracture analysis of quasi-brittle materials. Int J Mech Sci 2022;227:107445.
[15] Liu R, Xue S. Li Y. A three-dimensional (3D) micro-potential-based peridynamics model for deformation and fracture in solid materials. Eng Fract Mech 2023;282:109180.
[16] Silling SA, Lehoucq RB. Peridynamic theory of solid mechanics. Adv Appl Mech 2010;44:73–168.
[17] Huang D, Lu G, Qiao P. An improved peridynamic approach for quasi-static elastic deformation and brittle fracture analysis. Int J Mech Sci 2015;94-95:111–22.
[18] Silling SA, Bobaru F. Peridynamic modeling of membranes and fibers. Int J Non-linear Mech 2005;40:395–409.
[19] Bang DJ, Madenci E. Peridynamic modeling of hyperelastic membrane deformation. J Eng Mater Technol 2017;139:031007. -1.
[20] Yin B, Sun W, Zhang Y, Liew K. Modeling via peridynamics for large deformation and progressive fracture of hyperelastic materials. Comput Methods Appl Mech Eng 2023;403:115739.
[21] Bellido JC, Cueto J, Mora-Corral C. Bond-based peridynamics does not converge to hyperelasticity as the horizon goes to zero. J Elast 2020;141:273–89.
[22] Silling SA, Epton M, Weckner O, Xu J, Askari E. Peridynamic states and constitutive modeling. J Elast 2007;88:151–84.
[23] Breitenfeld MS, Geubelle PH, Weckner O, Silling SA. Non-ordinary state-based peridynamic analysis of stationary crack problems. Comput Methods Appl Mech Eng 2014;272:233–50.
[24] Behzadinasab M, Foster JT. A semi-Lagrangian constitutive correspondence framework for peridynamics. J Mech Phys Solids 2020;137:103862.
[25] Gu X, Zhang Q, Madenci E, Xia XZ. Possible causes of numerical oscillations in non-ordinary state-based peridynamics and a bond-associated higher-order stabilized model. Comput Methods Appl Mech Eng 2019;357:112592.
[26] Silling SA. Stability of peridynamic correspondence material models and their particle discretizations. Comput Methods Appl Mech Eng 2017;322:42–57.
[27] Chen H. Bond-associated deformation gradients for peridynamic correspondence model. Mech Res Commum 2018;90:34–41.
[28] Chen H, Spencer BW. Peridynamic bond-associated correspondence model: stability and convergence properties. Int J Numer Methods Eng 2019;117:713–27.
[29] Behera D, Roy P, Madenci E. Peridynamic correspondence model for finite elastic deformation and rupture in Neo-Hookean materials. Int J Non-Linear Mech 2020;126:103564.
[30] Roy P, Behera D, Madenci E. Peridynamic simulation of finite elastic deformation and rupture in polymers. Eng Fract Mech 2020;236:107226.
[31] Madenci E, Dorduncu M, Barut A, Phan N. Weak form of peridynamics for nonlocal essential and natural boundary conditions. Comput Methods Appl Mech Eng 2018;337:598–631.
[32] Chen Y, Yang Y, Liu Y. Large deformation and crack propagation analyses of hydrogel by peridynamics. Eng Fract Mech 2023;284:109261.
[33] Chen Y, Yang Y, Liu Y. Fatigue crack growth analysis of hydrogel by using peridynamics. Int J Fract 2023. https://doi.org/10.1007/s10704-023-00722-x.
[34] Bekar AC, Madenci E. Peridynamics enabled learning partial differential equations. J Comput Phys 2021;434:110193.
[35] Madenci E, Dorduncu M, Barut A, Futch M. Numerical solution of linear and nonlinear partial differential equations using the peridynamic differential operator. Numer Methods Partial Differ Equ 2017;33:1726–53.
[36] Madenci E, Barut A, Dorduncu M. Peridynamic differential operator for numerical analysis. New York: Springer; 2019.
[37] Haghighat E, Bekar AC, Madenci E, Juanes R. Anonlocal physics-informed deep learning framework using the peridynamic differential operator. Comput Methods Appl Mech Eng 2021;385:114012.
[38] Yu X, Zhou X. Adata-driven bond-based peridynamic model derived from group method of data handling neural network with genetic algorithm. Int J Numer Methods Eng 2022;123:5618–51.

[39] Ma JX, Zhou XP. Data-driven bond-based peridynamics with nonlocal influence function for crack propagation. Eng Fract Mech 2022;272:108681.
[40] You H, Yu Y, Silling SA, D'Elia M. Adata-driven peridynamic continuum model for upscaling molecular dynamics. Comput Methods Appl Mech Eng 2022;389:114400.
[41] Ning L, Cai Z, Dong H, et al. Physics-informed neural network frameworks for crack simulation based on minimized peridynamic potential energy. Comput Methods Appl Mech Eng 2023;417:116430.
[42] Babu JR, Gopalakrishanan S. Thermal diffusion in discontinuous media: a hybrid peridynamics-based machine learning model. Comput Struct 2024;290:107179.
[43] Li S, Jin Y, Lu H, et al. Wave dispersion and quantitative accuracy analysis of bond-based peridynamic models with different attenuation functions. Comput Mater Sci 2021;197:110667.
[44] Treloar LGR. The elasticity of a network of long-chain molecules–II. Trans Faraday Soc 1943;39:241–6.
[45] Mooney M. A theory of large elastic deformation. J Appl Phys 1940;11:582–92.
[46] Rivlin RS. Large elastic deformations of isotropic materials: I, fundamental concepts. II. Some uniqueness theorem for pure homogeneous deformation. Philos Trans R Soc A 1948;240:459–508.
[47] Zhang Q, Li S, Zhang AM, Peng Y, Yan J. A peridynamic Reissner-Mindlin shell theory. Int J Numer Methods Eng 2021;122:122–47.
[48] Li S, Lai X, Liu L. Peridynamic modeling of brittle fracture in Mindlin-Reissner shell theory. Comput Model Eng Sci 2022;131(2):715–46.
[49] Yeoh OH. Some forms of the strain energy function for rubber. Rubber Chem Technol 1993;66(5):754–71.
[50] Marquardt DW. An algorithm for least-squares estimation of nonlinear parameters. J Soc Ind Appl Math 1963;11(2):431–41.
[51] Hagan MT, Menhaj MB. Training feedforward networks with the Marquardt algorithm. IEEE Trans Neural Netw 1994;5(6):989–93.
[52] Gent AN. A new constitutive relation for rubber. Rubber Chem Technol 1996;69:59–61.
[53] Chen H, Spencer BW. Peridynamic bond-associated correspondence model: stability and convergence properties. Int J Numer Methods Eng 2018;117. https://doi.org/10.1002/nme.5973. 2019.
[54] Hu Y, Chen H, Spencer BW, Madenci E. Thermomechanical peridynamic analysis with irregular non-uniform domain discretization. Eng Fract Mech 2018;197:92–113.
[55] Tang JD, Li J, Vlassaka JJ, Suo ZG. Fatigue fracture of hydrogels. Extrem Mech Lett 2017;10:24–31.
[56] Rivlin RS, Thomas AG. Rupture of rubber. I. characteristic energy for tearing. J Polym Sci 1997;3:291–318.
[57] David R, Julie D, Mathis, et al. Critical strain energy release rate for rubbers: single edge notch tension versus pure shear tests. Int J Fract 2019;216:31–9.
[58] Zhang P, Xu ZY, Wu ZY, Xu P, Yang CH. Strengthening poly(2-hydroxyethyl methacrylate) hydrogels using biochars and hydrophobic aggregations. Int J Smart Nano Mater 2022. https://doi.org/10.1080/19475411.2022.2107115.
[59] Elsiddig E. An experimental method for estimating the tearing energy in rubberlike materials using the true stored energy. Sci Rep 2021;11:16229.
[60] Madenci E, Oterkus E. Peridynamic theory and its applications. New York: Springer; 2014.
[61] Zhang H, Qiao P. A state-based peridynamic model for quantitative fracture analysis. Int J Fract 2018;211:217–35.
[62] Yu H, Li S. On energy release rates in Peridynamics. J Mech Phys Solids 2020;142:104024.
[63] Madenci E, Oterkus S. Ordinary state-based peridynamics for plastic deformation according to von Mises yield criteria with isotropic hardening. J Mech Phys Solids 2016;86:192–219.
[64] Daniele D, Giulia S, Prasert P, et al. A stress tensor-based failure criterion for ordinary state-based peridynamic models. J Appl Comput Mech 2022;8(2):617–28.
[65] Ayatollahi MR, Heydari-Meybodi M, Dehghany M, Berto F. A new criterion for rupture assessment of rubber-like materials under Mode-I crack loading: the effective stretch criterion. Adv Eng Mater 2016;18(8):1364–70.
[66] Li XL, Li XJ, Sang JB, Qie YH. Experimental analysis of the damage zone around crack tip for rubberlike materials under mode-I fracture condition. Key Eng Mater 2013;561:119–24.